International Journal of Thermal Sciences 49 (2010) 170–181

Contents lists available at ScienceDirect

International Journal of Thermal Sciences

journal homepage: www.elsevier.com/locate/ijts

Characteristics of instability of radiation-induced natural convection in shallow littoral waters

Yadan Mao*, Chengwang Lei, John C. Patterson

School of Engineering, James Cook University, Townsville QLD 4811, Australia

ARTICLE INFO

Article history:
Received 20 January 2009
Received in revised form
29 June 2009
Accepted 7 July 2009
Available online 31 July 2009

Keywords:
Natural convection
Instability
Spectral analysis
Littoral waters
Mixing

ABSTRACT

Mixing and transport of terrestrially derived solutes and particulates in littoral regions depend heavily on the characteristics of flow instability. The criteria for radiation-induced instability to occur and the scope of the unstable region in near shore waters were revealed in our previously reported scaling analysis. In the present paper, the characteristics of instability of radiation-induced natural convection in shallow littoral regions are considered. Spectral analysis is conducted to reveal the frequency modes and the power of instability at various positions for different Rayleigh numbers. Results indicate that harmonic frequency modes are present at relatively low Rayleigh numbers. Both the power of instability and the prominence of higher frequency modes increase with offshore distance and the Rayleigh number for the considered shallow region. For a given offshore distance, the frequency modes of instability are the same over the local depth, but the prominence of higher frequency modes increases with depth. It is found that the scaling relation for the stable convection region specified in the previous investigation is also applicable to the time-averaged mean flow in the unstable region.

1. Introduction

The environmental effect of terrestrially derived solutes and particulates on the water quality in littoral regions has received considerable attention. The water body is self-resilient to some extent due to exchanges and mixing generated by various natural mechanisms, such as wind generated currents and waves [1], which help to reduce the residence time and the concentration of potential pollutants. Physical processes in littoral regions have been reported comprehensively in reviews in the context of physical limnology [2–4].

For littoral regions under relatively calm conditions, another natural mechanism becomes prominent in refreshing the water and is a subject of increasing recent interest; that is, the transport by convective circulations resulting from a spatial variation of the temperature field. Vertically, an adverse temperature gradient may result in thermal plumes that promote vertical transport, which is well known as Rayleigh–Bénard convection. Horizontally, a horizontal temperature gradient leads to a pressure gradient that drives a circulation, which is often referred to as a "thermal siphon", the significance of which in refreshing water has been demonstrated by field experiments [5–7]. It is revealed that the "thermal siphon" is a predominant mechanism driving the cross-shore circulation in relatively calm near-shore regions with limited wind-driven and tidal circulation. The "thermal siphon" has important biological and environmental implications, linking the coastal ecosystem with the adjacent ocean by transporting phytoplankton and other suspended matter [8,9], and affecting the eutrophication of reservoirs and lakes by exchanges of nutrients such as phosphorus, oxygen and other substances between the near-shore and the open water [10–12].

One intrinsic factor that induces a horizontal temperature gradient is the near shore geometry. As the depth of water increases in the offshore direction, the near shore geometry may be characterized by a triangular domain with a horizontal surface and a sloping bottom. A simple model has been proposed to explain the natural convection process [7,13,14]: an approximately equal amount of heating or cooling is uniformly distributed over a varying depth of water as the offshore distance varies, and thus the water at any given location becomes either hotter or cooler than its horizontal neighboring region, resulting in a horizontal temperature gradient that drives a circulation.

The simple model described above facilitates general understanding of the mechanism, but is insufficient to closely represent the reality in that it assumes a uniform distribution of thermal energy over the local depth. From a more physically realistic perspective, during daytime heating the water body absorbs solar radiation in an exponentially decaying manner with water depth

* Corresponding author. Tel.: +61 7 47815234; fax: +61 7 47816788.
E-mail address: yadan.mao@jcu.edu.au (Y. Mao).

1290-0729/$ – see front matter © 2009 Elsevier Masson SAS. All rights reserved.
doi:10.1016/j.ijthermalsci.2009.07.004

Nomenclature

A	bottom slope
C_p	specific heat, J/(kg °C)
$f_2(x)$	local critical function for instability
g	acceleration due to gravity, m/s^2
h	the maximum water depth, m
$H(x)$	non-dimensional horizontal heat transfer rate
H_0	heating intensity at the surface ($=I_0/(\rho C_p)$), m °C/s
I, I_0	radiation intensity at a given water depth and water surface, W/m^2
k	thermal diffusivity, m^2/s
$\hat{n}$	coordinate normal to the bottom, m
p	pressure, Pa
Pr	Prandtl number ($=\nu/k$)
$Q(x)$	non-dimensional flow rate
Ra	global Rayleigh number ($=g\beta H_0 h^4/(\nu k^2)$)
Ra_c	critical Rayleigh number ($=Ra_c(0^\circ)/\cos\theta$)
$Ra_c(0^\circ)$	critical Rayleigh number for horizontal fluid layers (≈ 1101)
S	internal heating source, °C/s
t_B	onset time of instability, s
T	local temperature, °C
T_0	average temperature, °C
T_1	temperature difference ($=T-T_0$) °C
u	velocity component in x-direction, m/s
v	velocity component in y-direction, m/s
x	coordinate in horizontal direction, m
x_0	dividing position between stable and unstable region, m
y	coordinate in vertical direction, m

Greeks

β	coefficient of thermal expansion, 1/°C
η	bulk attenuation coefficient for water, 1/m
ν	kinematic viscosity, m^2/s
ρ_0	density, kg/m^3
θ	inclination angle of the thermal layer, °

following Beer's law. Typically, the penetration depth of solar radiation is about 1–2 m in natural water bodies. Therefore, for the offshore region deeper than the penetration depth of solar radiation, the water body is stably stratified. For the shallow region near the shore, the residual radiation reaching the bottom slope is assumed to be absorbed by the bottom and the absorbed energy is re-emitted as a bottom heat flux [15–17]. Therefore, the bottom heat flux increases toward the shore, resulting in a horizontal temperature gradient that drives a flow up the bottom slope and outwards near the surface. In addition, the adverse temperature gradient near the bottom slope is a potential source for a Rayleigh–Bénard type instability, resulting in rising thermal plumes, which enhance direct vertical transport. The rising thermal plumes have been visualized using a shadowgraph technique in the laboratory experiments of Lei and Patterson [18]. Under natural conditions where the thermal forcing is varying smoothly over diurnal cycles, the existence of thermal plumes due to daytime heating by radiation has been demonstrated in the numerical simulation of Lei and Patterson [19].

The scaling analysis by Lei and Patterson [16] provides an overall description of flow states at different parametric settings. Subsequently, an improved scaling analysis of this problem by Mao et al. [17] has revealed the variation of flow properties with offshore distance, which was verified by numerical simulations. It is reported by Mao et al. [17] that, for relatively large bottom slopes and sufficiently high Rayleigh numbers, the entire flow domain can be divided into three sub-domains, with the dominant mode of horizontal heat transfer changing from conduction into stable convection and finally into unstable convection as offshore distance increases. Detailed scaling was provided for the properties of the thermal flow in the conduction and convection dominated regions respectively with offshore distance included as a variable. The scaling in [17] revealed the extent of the unstable region and the occurrence time for instability at varying offshore distances. Although revealing further stability properties of the unstable region was beyond the capability of the scaling described above, inspired by the scaling, it is expected that the power spectrum of the time series of flow properties may vary with offshore distance as well, which will provide insight into the variation of mixing and transport with offshore distance.

Linear stability analysis is often performed to reveal the critical condition for instability to occur and the critical wave-number at the onset of the instability. Assuming longitudinal rolls as the form of instability, Farrow and Patterson [20] conducted a linear stability analysis of an asymptotic base flow with the bottom slope approaching zero, in which the critical Rayleigh number for instability was derived as a function of the offshore distance. The critical Rayleigh number function of Farrow and Patterson [20] is in qualitative agreement with the scaling results of Mao et al. [17]. However, the linear stability analysis is unable to characterize the instability properties at a more developed stage of the flow development. As the base flow and the flow instability develop with time, the effect of non-linearity becomes increasingly significant and thus cannot be ignored. In fact, the 3-D numerical simulation results of Lei and Patterson [21] reveal that the form of instability evolves with time as the flow develops and is more complicated than simple longitudinal rolls.

For the unstable regime, the flow development can be classified into three stages: initial, transitional and quasi-steady [16,17]. The stability properties of the flow in the initial and early-transitional stages were investigated by Lei and Patterson [21] using direct stability analysis based on 3-D numerical simulations, which revealed the variation of certain instability properties (the onset time of instability, the transverse wave number and the growth rate of instability) with offshore distance. The variation of the onset time of instability with offshore distance revealed by the direct stability analysis was in agreement with the scaling analysis by Mao et al. [17]. However, the direct stability analysis by Lei and Patterson [21] focused only on the stability properties of the flow at the initial and early-transitional stage but not the stability properties at the quasi-steady state. Spectral analysis of the time series during the quasi-steady state indicates that the frequency modes of the fluctuations and their respective power remain approximately constant as briefly described in Mao et al. [17].

In this paper, in order to reveal the detailed stability properties of the radiation-induced natural convection at quasi-steady state, spectral analysis is conducted over a period corresponding to the quasi-steady state. Inspired by the above literature, it is expected that the spectrum may vary with offshore distance, and thus spectral analysis is conducted at various offshore distances for the quasi-steady state flow.

It is reported that for the case of an inclined cavity or an infinite inclined heated wall of a small slope, longitudinal rolls are the preferred mode of instability [22–24]. However, for the present configuration of a triangular domain with a non-uniformly heated sloping bottom, both the 3-D simulation [21] and the laboratory experiment [18] indicate that for $Ra \sim 10^6$, instabilities are present at the quasi-steady state in the form of thermal plumes, involving a transverse wave number. Here we focus on the qualitative variation of spectral properties with offshore distance, the direction of which is included in the 2-D model. Therefore, the adopted 2-D model is adequate for the purpose of the present investigation. Comparisons between the 2-D and 3-D simulation results suggest that the 2-D results are representative of the longitudinal profile of the 3-D results at all stages of the flow development [25].

The purpose of the present investigation is to reveal the characteristics of instability in the transitional flow regime, providing some insight into the transition from laminar to turbulent flows, and thus turbulence modeling is outside the scope of this paper. The numerical simulation conducted in this paper adopts a constant molecular viscosity for water, and the Rayleigh numbers are limited to the order of $10^6 \sim 10^7$, approaching the transition from laminar to turbulent flow. In addition, the present investigation considers the near-shore shallow water region where the maximum water depth is less than the penetration depth of radiation ($h < 1/\eta$), which is about 1–2 m in natural water bodies. In this case, the effect of the bottom heat flux resulting from the absorption of radiation by the sloping bottom is strong. Further offshore, as the water depth increases, the radiation reaching the sloping bottom gradually becomes negligible.

2. Model formulation

The daytime circulation near the shore is modelled with a wedge with a bottom slope of A and a maximum water depth of h (Fig. 1). With the Boussinesq assumption, the Navier–Stokes and energy equations governing the flow and temperature evolution within the wedge are written as:

$$\frac{\partial u}{\partial x} + \frac{\partial v}{\partial y} = 0 \tag{1}$$

$$\frac{\partial u}{\partial t} + u\frac{\partial u}{\partial x} + v\frac{\partial u}{\partial y} = -\frac{1}{\rho_0}\frac{\partial p}{\partial x} + \nu\nabla^2 u \tag{2}$$

$$\frac{\partial v}{\partial t} + u\frac{\partial v}{\partial x} + v\frac{\partial v}{\partial y} = -\frac{1}{\rho_0}\frac{\partial p}{\partial y} + \nu\nabla^2 v + g\beta(T - T_0) \tag{3}$$

$$\frac{\partial T}{\partial t} + u\frac{\partial T}{\partial x} + v\frac{\partial T}{\partial y} = k\nabla^2 T + S \tag{4}$$

The radiation intensity at a particular wavelength decreases with the water depth according to Beer's law [26]:

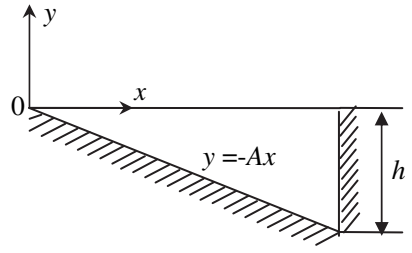

Fig. 1. Geometry of the flow domain.

$$I = I_0 e^{\eta y} \quad y \le 0 \tag{5}$$

The absorption of radiation is often assumed to be characterized by a single attenuation coefficient in most limnological applications to simplify the problem, and this assumption is also adopted here. Therefore, the source term in Eq. (4) is given by:

$$S = H_0 \eta e^{\eta y} \quad -Ax \le y \le 0 \tag{6}$$

In the present model, a rigid non-slip boundary condition is assumed for the bottom slope ($u = v = 0$) and the deep-end wall, and the water surface is assumed to be stress free ($\partial u/\partial y = 0$ and $v = 0$). An adiabatic temperature condition is assumed for the water surface and the end wall. It is assumed that the bottom slope absorbs the radiation energy reaching the slope and re-emits the absorbed energy as a bottom heat flux:

$$\frac{\partial T}{\partial \hat{n}} = -\frac{1}{k} H_0 e^{-A\eta x} \tag{7}$$

The temperature of the water body increases through both direct absorption of radiation and the bottom heat flux. The former thermal forcing results in a stable stratification of water body, and thus no flow is generated through this mechanism. On the contrary, a thermal boundary layer adjacent to the bottom slope is generated through the latter mechanism, and within this boundary layer, a horizontal temperature gradient drives the water up the slope. In addition, an adverse vertical temperature gradient is present near the bottom slope, which is a potential source for thermal instability.

3. Extent of the unstable region

To investigate the characteristics of flow instability, it is essential to ascertain the extent of the unstable region. Mao et al. [17] have provided and verified the scaling for the extent of distinct regions dominated by different modes of heat transfer: conduction, stable convection and unstable convection. Results that involve the criteria for instability and the extent of instability, which are directly relevant to the present investigation, are briefly summarised below.

For any local horizontal position x, a critical Rayleigh number function for instability to occur is derived in [17] as

$$f_2(x) \sim Ra_c^3 (h/x)^4 e^{A\eta x}, \tag{8}$$

where Ra_c can be approximated by [27]:

$$Ra_c = Ra_c\left(0^\circ\right)/\cos\theta, \tag{9}$$

For shallow waters where $h < 4/\eta$, $f_2(x)$ decreases monotonically in the offshore direction. Instability occurs if

$$f_2(x) < Ra, \tag{10}$$

From (8) and (10), it follows that instability occurs if

$$Ra > f_2(x)_{\min} \sim Ra_c^3 A^4 e^{\eta h}, \tag{11}$$

The function $f_2(x)$ becomes infinite as $x \to 0$, indicating that there is always a stable region near shore.

As revealed by Mao et al. [17], in the unstable flow regime, the dominant mode of horizontal heat transfer changes from conduction to stable convection and finally to unstable convection as the offshore distance increases. The position x_0 that divides the unstable region offshore from the stable region near shore is determined from

$$f_2(x_0) \sim Ra \tag{12}$$

Given the complex nature of the $f_2(x)$ function (refer to (8)), no explicit form of x_0 can be obtained from (12). However, x_0 can be easily determined numerically from (12).

The time for instability to set in is scaled in [17] as:

$$t_B \sim \left(\frac{Ra_c}{Ra}\right)^{1/2} \frac{h^2}{k} e^{\frac{A\eta x}{2}} \tag{13}$$

With the guidance of the above scales, the following sections will focus on the characteristics of instability within the unstable region at quasi-steady state for shallow waters with relatively large bottom slopes ($A > Ra_c^{-1/2}$) as classified in [17], in particular, the variation of spectral properties with horizontal position x and the Rayleigh number.

4. Numerical procedures

In the numerical simulations, an end-wall is assumed at the deep end so that the calculations can be carried out within a finite domain. The end-wall results in an abrupt change in the boundary condition and a return flow which will affect the stability property near the end-wall. Therefore, subsequent discussion will focus on the region relatively far from the end-wall to avoid its effect. Furthermore, the adoption of a rigid wall at the deep end indicates that the cross-shore exchange flow at the position of the endwall is not considered here.

With a constant radiation being applied at the water surface and no heat loss through any boundaries, the temperature of the water body will continue rising. In this sense, there is no steady or quasi-steady state with respect to temperature. However, a quasi-steady state will be reached with respect to the flow velocity and temperature gradient. At the quasi-steady state, the temperature increases at the same rate everywhere, and thus the difference between the local temperature and the average temperature becomes steady.

As noted in [16], the average temperature of the flow can be derived from the energy entering into the water body and the energy absorbed by the water body.

$$T_0 = \frac{2H_0}{h} t \tag{14}$$

The equation governing the variation of the temperature difference T_1 between the local temperature T and the average temperature T_0 can be derived from equation (4) as:

$$\frac{\partial T_1}{\partial t} + u\frac{\partial T_1}{\partial x} + v\frac{\partial T_1}{\partial y} = k\nabla^2 T_1 + H_0\left(\eta e^{\eta y} - \frac{2}{h}\right), \tag{15}$$

Replacing equation (4) with equation (15) results in a new set of equations for T_1. Thus, the problem of constantly increasing temperature T is converted to a quasi-steady problem for T_1. In the unstable flow regime, at quasi-steady state, the time series of T_1 and other flow properties fluctuates around a certain constant value. The thermal boundary conditions for T also apply to T_1 since only temperature gradients are involved in these conditions. The non-dimensional form for the new set of governing equations is written as:

$$\frac{\partial u}{\partial x} + \frac{\partial v}{\partial y} = 0 \tag{16}$$

$$\frac{\partial u}{\partial t} + u\frac{\partial u}{\partial x} + v\frac{\partial u}{\partial y} = -PrRa\frac{\partial p}{\partial x} + Pr\nabla^2 u, \tag{17}$$

$$\frac{\partial v}{\partial t} + u\frac{\partial v}{\partial x} + v\frac{\partial v}{\partial y} = -PrRa\frac{\partial p}{\partial x} + Pr\nabla^2 v + PrRaT_1, \tag{18}$$

$$\frac{\partial T_1}{\partial t} + u\frac{\partial T_1}{\partial x} + v\frac{\partial T_1}{\partial y} = \nabla^2 T_1 + (\eta e^{\eta y} - 2). \tag{19}$$

In Equations (16)–(19) and hereafter, all the quantities are non-dimensional which have been normalized with the following scales: the length scale x, y, $1/\eta \sim h$; the time scale; $t \sim h^2/k$; the temperature scale $T_1 \sim H_0 h/k$; the velocity scale: $u, v \sim k/h$; and the pressure gradient scale: $p_x, p_y \sim \rho_0 g\beta H_0 h/k$.

The non-dimensional form of the governing equations (16)–(19) along with the specified boundary and initial conditions are solved numerically using a finite volume method. The SIMPLE scheme is adopted for pressure-velocity coupling; and the QUICK scheme is applied for spatial derivatives. A second-order implicit scheme is applied for time discretization in calculating the transient flow.

The simulation is conducted in a triangular domain of a dimensionless depth of $h = 1$, a length of $x = 10$ and a bottom slope of $A = 0.1$, with a non-dimensional attenuation coefficient of $\eta = 0.12$ and a Prandtl number of $Pr = 7$. In order to avoid a singularity at the tip, the tip is cut off at $x = 0.2$, and an extra non-slip and adiabatic vertical wall is assumed there. The cut region accounts for only 0.04% of the full domain, and thus no significant modification to the flow is anticipated.

For the spectral analysis of the numerical results, in addition to the flow properties at discrete locations, two integral parameters of practical significance have been calculated from the simulation results: the average volumetric flow rate $Q(x)$ over the depth which characterizes the strength of the flow at a horizontal position x, and the average horizontal convection rate $H(x)$ over the depth which characterizes the strength of horizontal heat transfer at the horizontal position x. These two quantities are calculated as

$$Q(x) = \frac{1}{2Ax}\int_{-Ax}^{0} |u| \mathrm{d}y, \tag{20}$$

$$H(x) = \frac{1}{Ax}\int_{-Ax}^{0} uT_1 \mathrm{d}y, \tag{21}$$

where $Q(x)$ is normalized by k/h and $H(x)$ is normalized by I_0.

5. Results and discussions

From scale (11), it follows that for the current parametric settings, the Rayleigh number needs to be larger than $\sim 1.5 \times 10^5$ in order for instability to occur. In this study, we consider Rayleigh numbers in the range of 1.4×10^6 to 1.4×10^7 for the unstable cases. A mesh and time step dependency test has been conducted for $Ra = 1.4 \times 10^7$ with three different meshes, 211×71, 315×105 and 421×141. The time steps for different meshes are adjusted accordingly so that the CFL (Courant–Freidrich–Lewy) number remains approximately the same for all the meshes. Since the spectra at different positions are the focus of this paper, the influence of mesh resolution on the spectrum of the vertical velocity v at $x = 4.0$, $y = -0.3$ is examined. Fig. 2 shows the spectra of the vertical velocity over a dimensionless time period of 0.1 at the quasi-steady state obtained with different meshes. In Fig. 2 and all subsequent spectral figures, the frequency has been normalized by k/h^2. The spectrum variation among different meshes suggests that the spectrum is sensitive to the density of the mesh, which is in fact one of the features of the transition from laminar to turbulent flow. Higher frequencies are more prominent in denser grids. However, the numerical results presented in Table 1 suggest that the numerically predicted values of major stability properties are converging as the mesh density increases. Furthermore, the Rayleigh number tested here is the highest among all the calculated cases; the effect of the grid

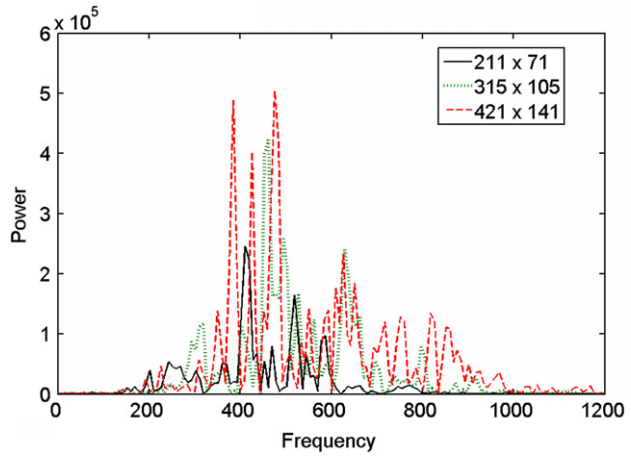

Fig. 2. Spectra of the time series of the vertical velocity v at $x = 4.0$, $y = -0.3$ for $Ra = 1.4 \times 10^7$ from different meshes.

resolution on the solution is expected to be less significant for other cases with lower *Ra*. In order to ensure the accuracy of the solutions, the grid 421×141 is used in all the following simulations. For the chosen mesh, the minimum face area is 0.0024; the maximum is 0.5125; and the maximum stretch factor is 1.07. The time step adopted for this mesh is 2.0×10^{-5}, giving a maximum CFL number of 1.02 for the present Rayleigh number.

5.1. Spatial pattern of instability

For investigating instability, contours such as streamlines or isotherms reveal the spatial pattern of instability, such as the wavelength and the relative power of fluctuation in a spatial perspective, whereas analysis of temporal data for any given position reveals the dominant frequencies and power of the corresponding modes of instability in a temporal perspective. A combined analysis of both temporal records and spatial features provides a deeper insight into the nature of instability. Fig. 3 shows the spatial features of the thermal flow over the entire domain at a particular time of the quasi-steady state for a typical Rayleigh number (2.1×10^6) in the unstable regime. The anticlockwise flow near the deep end of the domain (Fig. 3a) is caused by an end-effect of the vertical wall. The extents of the wavy features in the streamlines (Fig. 3a), the isotherms (Fig. 3b) and the horizontal heat transfer rate (Fig. 3c) correspond well. Both the streamlines and isotherms suggest that over a large offshore region, thermal plumes rise up from the bottom boundary layer. It is also clear that these plumes do not penetrate all the way through to the top surface and they are more pronounced in the far offshore region, indicating increasing power of instability in offshore direction. These qualitative features revealed by the temperature and flow structures will be further investigated quantitatively using the time series of thermal properties.

Table 1
Spectral and statistical properties of the vertical velocity v at $x = 4.0$, $y = -0.3$ for different grids.

	1. 211×71	2. 315×105	3. 421×141	Variation 1 & 2	Variation 2 & 3
f_d	410.8	461.1	475.7	11.5%	3.1%
P_d	2.5×10^5	4.2×10^5	5.0×10^5	50.8%	17.4%
Std	52.3	58.8	60.7	11.7%	3.2%
Mean	23.6	22.9	22.5	3.0%	1.8%

Note: 'f_d' denotes the most dominant frequency, 'P_d' denotes the power of the most dominant frequency. "std" denotes the standard deviation of the time series at quasi-steady sate. "mean" demotes the vertical velocity v averaged over the time series during quasi-steady state.

5.2. Identification of the quasi-steady state

To investigate the stability at the quasi-steady state, the period of time corresponding to the quasi-steady state needs to be identified by analysing the time series of flow properties. Fig. 4 shows the time series of the horizontal velocity at the point $x = 4.33$ and $y = 0.4$, which is near the bottom slope. The entire range of the time series is shown in logarithmic and linear time scales in Fig. 4(a) and (b) respectively, with the different stages of the flow development roughly identified. It is seen in Fig. 4 that the magnitude of flow velocity increases smoothly during the stable development stage. Once instability sets in, the flow velocity begins to fluctuate with time, indicating the start of the transitional stage. The characteristics of the fluctuation vary throughout the transitional stage. At the early transitional stage, the fluctuation is irregular and varies largely in magnitude. From the early transitional stage to the middle transitional stage, the magnitude of fluctuation gradually decreases and the fluctuation is superimposed on a more stable value. In the late transitional stage, the fluctuation becomes more regular and the magnitude is smaller than that in the middle transitional stage. As shown in Fig. 4(c), the dominant frequency mode shifts toward the higher end of the spectrum as the flow develops with time. Finally, the flow reaches the quasi-steady state which is characterized by regular fluctuations with fixed dominant frequencies, as shown in Fig. 4(d). Analysis of other flow properties, e.g. the vertical velocity and temperature, shows the same sequences of flow development. With the quasi-steady state identified in the time series, the spectral analysis in the following sections is conducted based on the quasi-steady section of the time series.

5.3. Spectral variation with water depth

Before investigating the spectral variation with the offshore distance, it is interesting to reveal the spectral variation with local depth at a given horizontal position. For this purpose, spectral analysis is conducted based on flow properties at different local depths for a given horizontal position.

As shown in Fig. 3, thermal plumes are rising up from the bottom, and thus the vertical velocity is expected to be sensitive to the rising plumes. For a given Rayleigh number and a horizontal position x, spectral analysis is conducted on the time series of the vertical velocity for different vertical positions. Two exemplary sets of spectra for two different Rayleigh numbers are shown in Fig. 5(a) and (c) respectively. It is clear in these figures that, although the power of fluctuation varies with the depth, the major frequency modes of the vertical velocity are the same for different depths. Spectral analysis on other flow properties, such as temperature and horizontal velocity suggests the same trend. Therefore, it is expected that the frequency modes of integrated flow properties over the local depth, such as $H(x)$ and $Q(x)$ defined in (22) and (23), are representative of the frequency modes for different depths at the horizontal position x.

To reveal the variation of the dominancy of different frequency modes with water depth, the spectrum obtained at a given water depth is normalized by the maximum power of the respective spectrum. Similar treatment to the spectra is done for a number of water depths at a given horizontal position, and a frequency mode map is then constructed from these normalized spectra over different water depths. These are shown for two different Rayleigh numbers in Fig. 5(b) and (d) respectively. As shown in the legend,

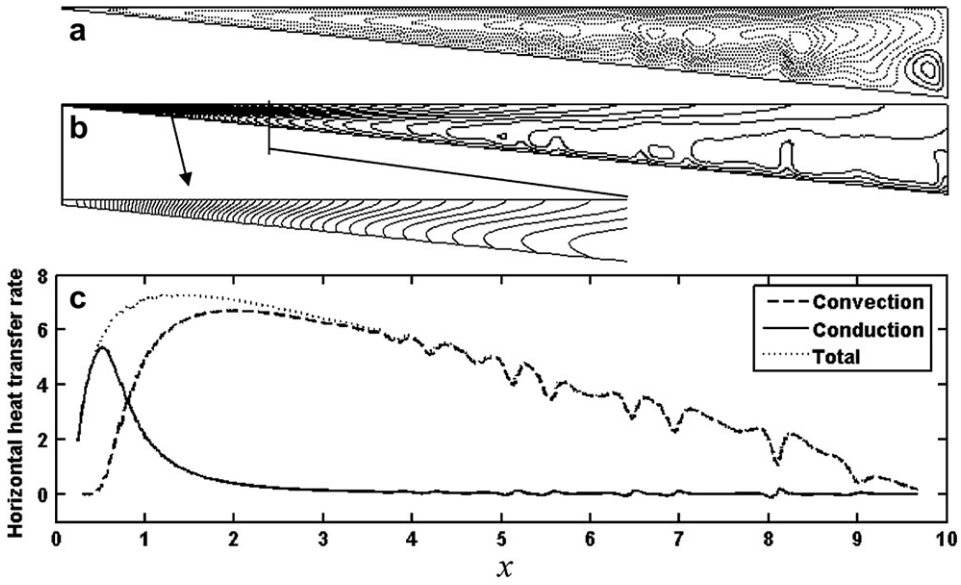

Fig. 3. Spatial Features of instability at $Ra = 2.1 \times 10^6$ (a) streamlines with an interval of 3.5; dashed lines indicate clockwise flow and solid lines indicate anti clockwise flow (b) temperature contours with an interval of 0.028; the extent of the enlarged view is up to $x = 2.35$ with a contour interval of 0.070 (c) the horizontal convective, conductive and total heat transfer rates averaged over the local water depth.

for a given water depth, corresponding to the colour change from blue to red, the power of the spectra varies from 'zero' to the maximum value at the respective depth, which becomes 'one' after normalization. For reference, the maximum power as a function of water depth is plotted beneath each of the spectral plots. Although the basic frequency modes are the same for different depths, the dominancy of each mode varies with water depth. Both Fig. 5(b) and (d) suggest that, as water depth increases, the dominant frequency mode shifts from low to higher frequencies. It is also interesting that, the maximum power, which represents the power of the most dominant frequency mode, first increases and then decreases with the water depth.

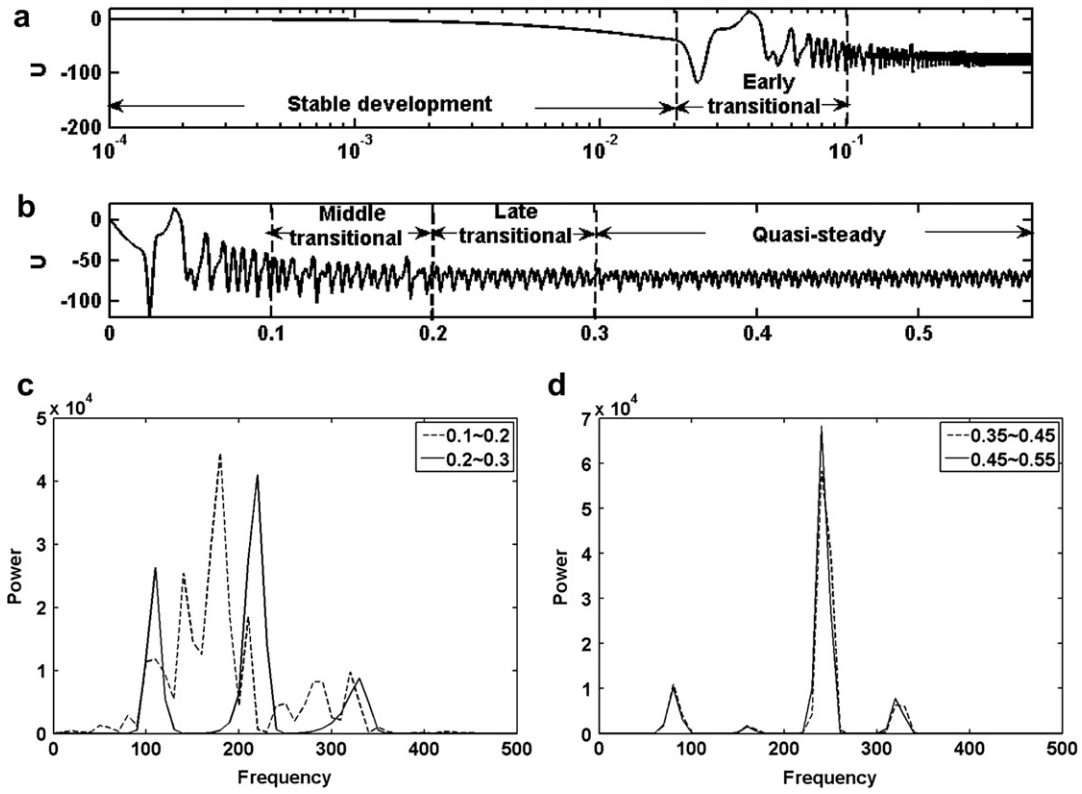

Fig. 4. Time series of horizontal flow velocity at the position of (4.33, 0.4) and spectra of different sections of the time series. (*a*) Time series with a linear time scale. (*b*) Time series with a logarithmic time scale. (c) Spectra before quasi-steady state. (d) Spectra during the quasi-steady state.

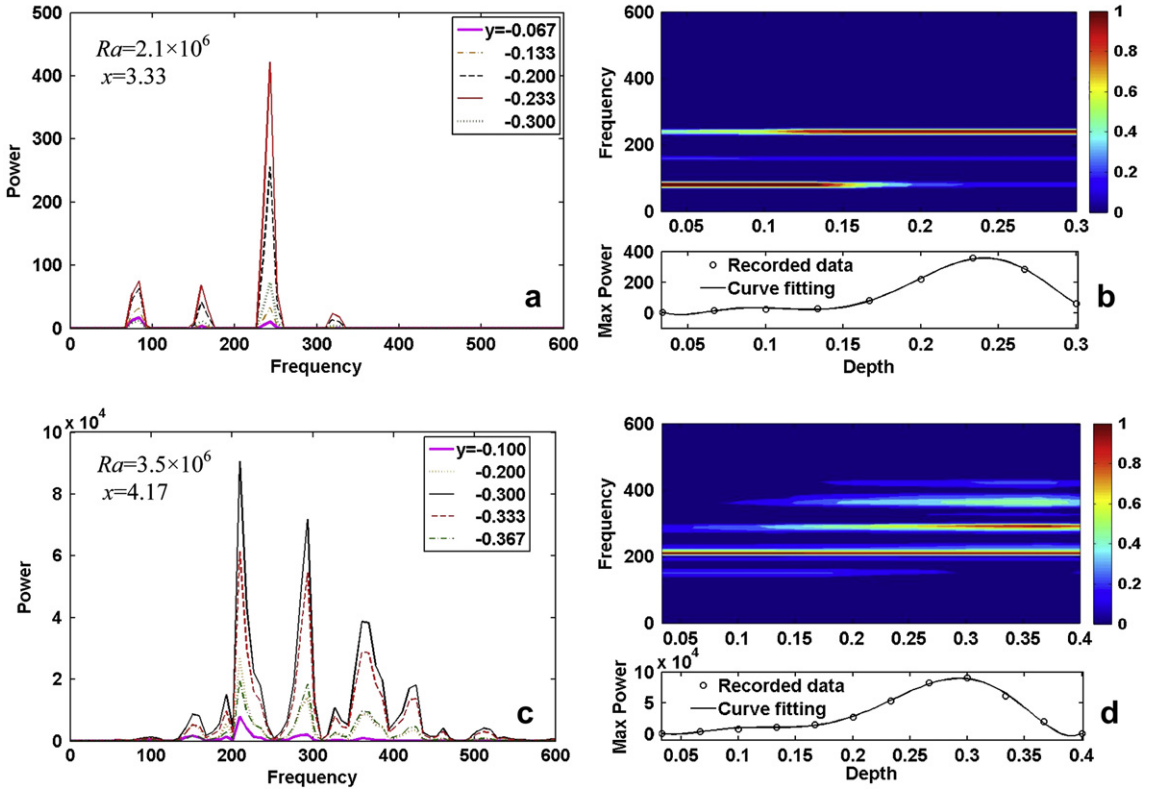

Fig. 5. Spectra of vertical velocity at various depths. (*a*) Spectra at various depths along the line of $x = 3.33$ for $Ra = 2.1 \times 10^6$. (*b*) Normalized spectra along $x = 3.33$ for $Ra = 2.1 \times 10^6$. (*c*) Spectra at various depths along the line of $x = 4.17$ for $Ra = 3.5 \times 10^6$. (*d*) Normalized spectra along $x = 4.17$ for $Ra = 3.5 \times 10^6$.

To illustrate the variation of the power of velocity fluctuation with water depth, the standard deviations of the time series of the vertical velocity, which are indicative of the intensity of instability, are plotted for different water depths in Fig. 6(a) and (b) for the two different Rayleigh number cases shown in Fig. 5 respectively. It is clear that from the water surface downwards, the intensity of the instability increases until reaching a maximum at a position close to the bottom, and then decreases with increasing depth, which is consistent with the variation of the maximum spectral power shown in Fig. 5(b) and (d). In the course of thermal plume development, the adverse temperature gradient in the thermal layer above the bottom slope motivates the formation of the plume, whereas fluid viscosity and stable stratification in the upper region tend to suppress its development. The power of the flow instability is dependent upon the balance among these different forces. As will be confirmed in Section 5.5, the position with the strongest power of instability is near the bottom slope, representing a region of active vertical mixing.

Comparison between the spectra of Fig. 5(a) and (c) suggests that the characteristics of the two sets of spectra are different: Fig. 5(a) shows harmonic modes of frequency, whereas the frequency bands in Fig. 5(c) are connected with each other and are not harmonic, indicating the trend of transition to turbulence as the Rayleigh number increases.

5.4. Spectral variation with offshore distance

Time series of the horizontal convection rate $H(x)$ averaged over the local depth are plotted in Fig. 7(a) and (b) for $Ra = 2.1 \times 10^6$ at $x = 3.33$ and 4.17 respectively. Comparison between Fig. 7(a) and (b) suggests that the amplitude of the fluctuation increases with x, indicating an increasing intensity of instability with the offshore distance. The increase of the intensity of instability with offshore distance can also be observed in the experimental results of Lei and Patterson (2002) in the region away from the end-wall by comparing the amplitude of fluctuations of the temperature time series at $x = 150$ mm and $x = 250$ mm.

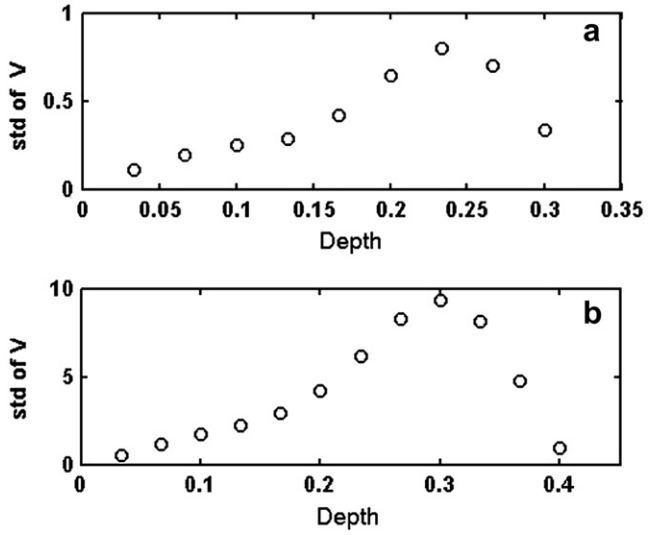

Fig. 6. Standard deviation of the time series of the vertical velocity during the quasi-steady state at various water depths: (*a*) $x = 3.33$ for $Ra = 2.1 \times 10^6$. (*b*) $x = 4.17$ for $Ra = 3.5 \times 10^6$.

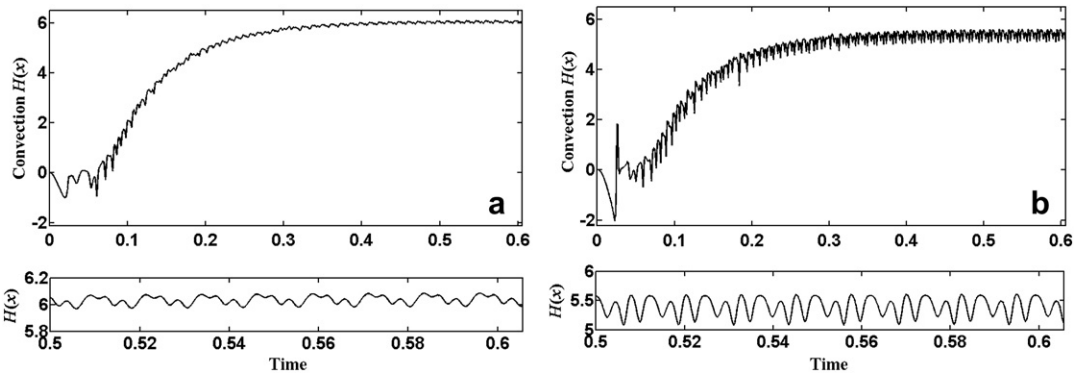

Fig. 7. Time series of the horizontal convection averaged over the local depth for $Ra = 2.1 \times 10^6$ (a) $x = 3.33$ (b) $x = 4.17$. The lower plots of (a) and (b) are the zoomed views of the time series at the quasi-steady state.

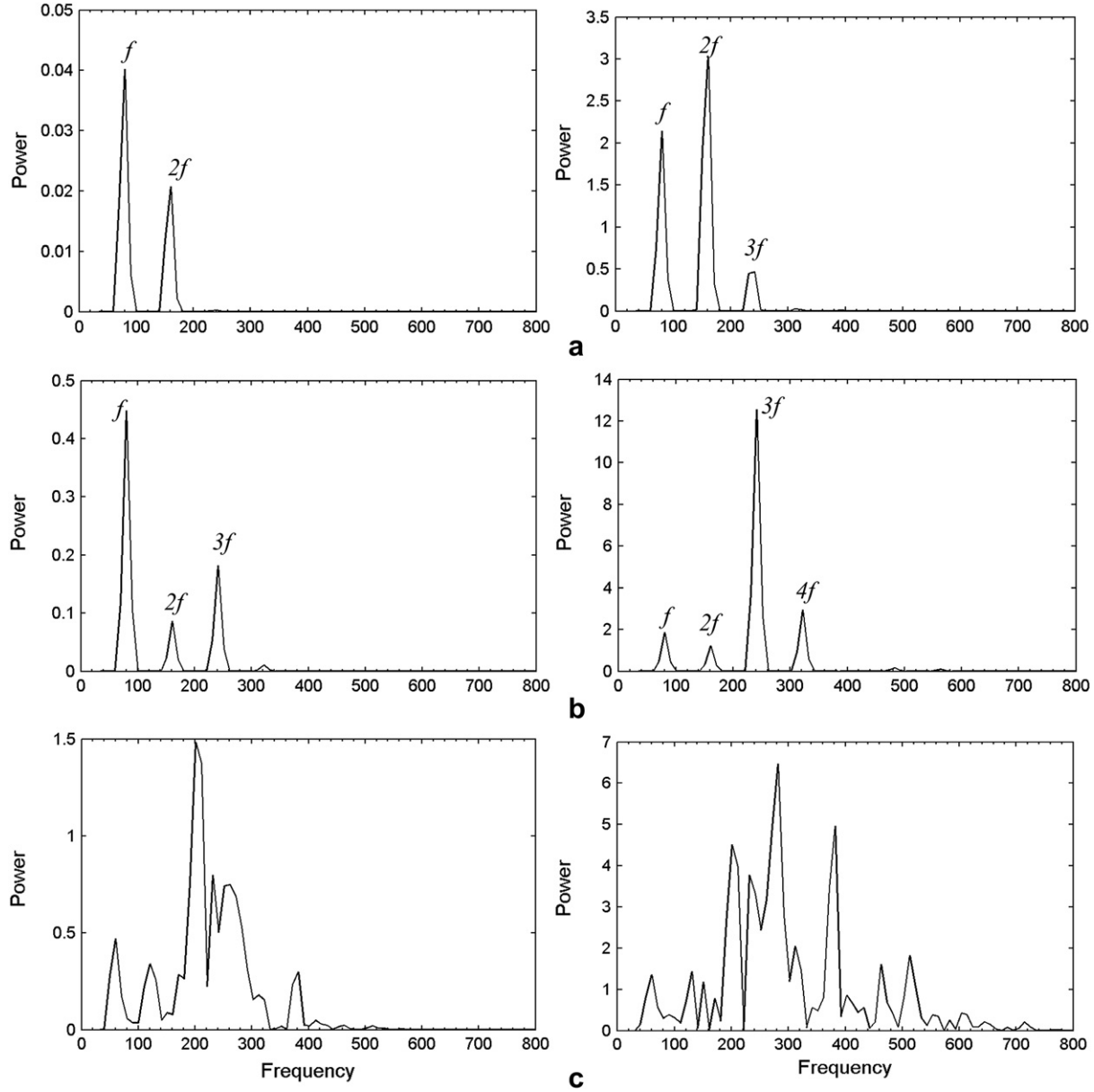

Fig. 8. The spectra of time series of horizontal convection $H(x)$ at the quasi-steady state at $x = 3.33$ (left) and $x = 4.17$ (right) for different Rayleigh numbers. (a) $Ra = 1.4 \times 10^6$ (b) $Ra = 2.1 \times 10^6$ (c) $Ra = 3.5 \times 10^6$.

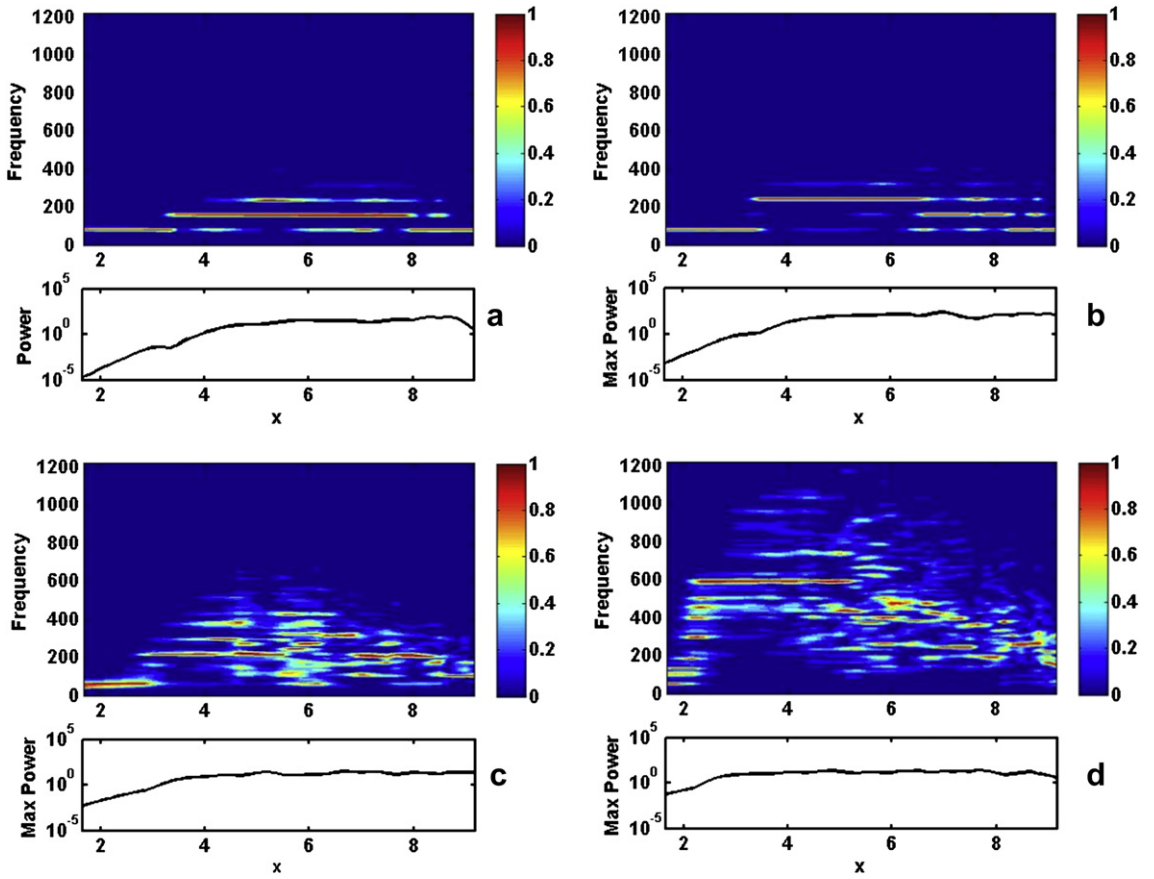

Fig. 9. Spectra of horizontal convection $H(x)$ normalized by the maximum power of each x position for different Rayleigh numbers. (a) $Ra = 1.4 \times 10^6$ (b) $Ra = 2.1 \times 10^6$ (c) $Ra = 3.5 \times 10^6$ (d) $Ra = 1.4 \times 10^7$.

The variation of the frequency modes and the power of the corresponding modes with offshore distance would be revealed by spectral analysis of the time series. Fig. 8 shows the results of spectral analysis of the time series of $H(x)$ over a dimensionless time period of 0.1 at the quasi-steady state obtained at two different horizontal positions $x = 3.33$ and 4.17 and for three Rayleigh numbers of $Ra = 1.4 \times 10^6$, 2.1×10^6 and 3.5×10^6 respectively.

Comparison between the left and the right figures in Fig. 8 suggests that for a given Rayleigh number, the prominence of high frequency modes increases with offshore distance and the power of all frequency modes also increases with the offshore distance. For $Ra = 1.4 \times 10^6$ and 2.1×10^6, the spectra are of distinct harmonic mode with the lowest frequency of $f = 80.5$. For $Ra = 3.5 \times 10^6$, the spectrum becomes more complex with the frequency bands connected with each other, suggesting that the interaction between different frequency modes becomes stronger as the Rayleigh number increases. The above analysis suggests that within the unstable flow regime, there is a transition from harmonic frequency modes to non-harmonic frequency modes as the Rayleigh number increases.

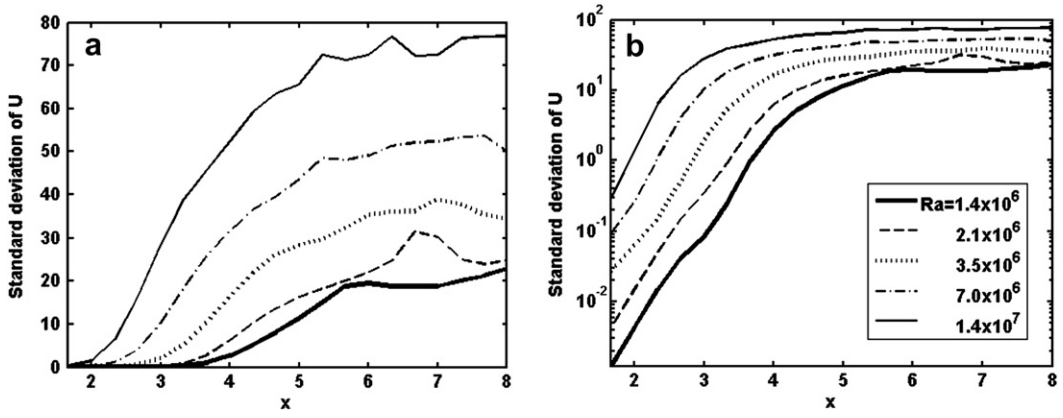

Fig. 10. Standard deviation of velocity component parallel to the bottom slope along $y = -0.1x + 0.33$ for different Rayleigh numbers. (a) Linear scale (b) Logarithmic scale.

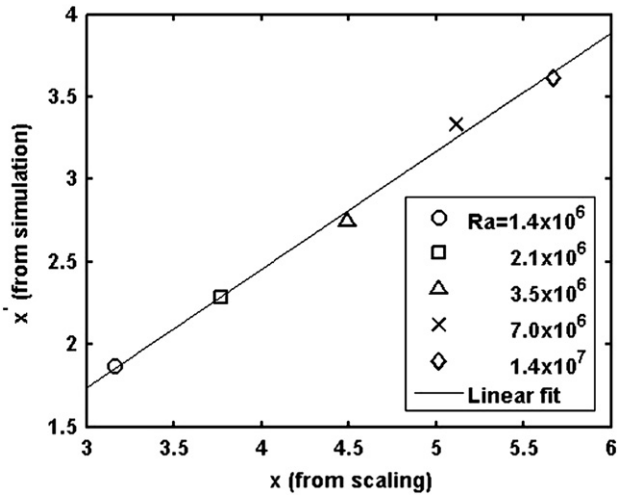

Fig. 11. Dividing positions between stable and unstable region predicted by scaling versus those from numerical simulations.

Although Fig. 8 reveals interesting spectral variation with the offshore distance, further investigation is needed so that a full picture of the spectral variation over a wide range of offshore distance can be revealed. Since the magnitude of the maximum spectral power varies significantly with offshore distance, as shown in Fig. 8, the spectra at various offshore distances are normalized by the maximum power of the respective spectrum, and a frequency mode map showing the spectral variation with offshore distance is generated. This is shown in Fig. 9. For reference, the maximum power as a function of offshore position is plotted beneath each of the spectral plots.

It is clear in Fig. 9 that for a given Rayleigh number, as offshore distance increases, the maximum power increases and the dominant frequency modes shifts in a step way to higher frequencies except for the end region which is affected by the end-wall. In the region affected by the end wall, the above described variation of dominant frequencies with offshore distance does not apply, and the frequency modes become complicated, which is expected since both the return flow imposed by the end wall and the abrupt change in boundary conditions alter the stability property of the flow near the end wall. A comparison of the spectra for different Rayleigh numbers in Fig. 9 suggests that as the Rayleigh number increases, both the number of frequency modes and the highest dominant frequency increase. In addition, as the Rayleigh number increases, the region dominated by high frequency modes, which are of high maximum power, expands toward the shore, indicating the expansion of unstable region. A similar trend of spectral variation is also found for the integrated volumetric flow rate $Q(x)$.

To further reveal the intensity variation of the instability with offshore distance and the Rayleigh number, the standard deviation of the velocity component parallel to the bottom slope is shown in Fig. 10 on both linear and logarithmic scales. It is clear that except for the region affected by the end wall, the intensity of instability increases with offshore distance, which is in agreement with the trend of increasing strength of the plumes with offshore distance observed from the spatial patterns of isotherms and streamlines in Fig. 3. A comparison of the standard deviation for $Ra = 2.1 \times 10^6$ in Fig. 10(a) with the spatial patterns in Fig. 3 indicates that the horizontal position where the standard deviation starts to increase noticeably with offshore distance corresponds to the position where the wavy feature becomes evident in the spatial pattern. The same feature is found for other Rayleigh numbers. Therefore, the analysis from the temporal and the spatial perspectives agree well with each other. In addition, Fig. 10 suggests that as the Rayleigh number increases, the region with intensive instability extends further toward the shore.

The positions where the standard deviation of horizontal convection starts to exceed a certain threshold were obtained in the previous investigation [17]. This position approximately represents the boundary between the stable and unstable regions and was plotted against the scaling prediction in [17]. Good linear correlation between the numerical data and the scaling prediction confirmed the scaling prediction of the dividing position between the stable and the unstable region. Here, a similar approach is taken to determine the dividing positions between the stable and unstable regions based on the standard deviation of the time series of the velocity component shown in Fig. 10, and the numerical results are plotted against the scaling prediction in Fig. 11. It is worth noting that the dividing positions obtained from the present numerical simulations are consistently smaller than those reported in [17]. This is caused by different thresholds for different flow properties adopted in determining the presence of instability between the present investigation and the previous one [17]. Despite the slight variation of the reported dividing positions from the previous study, a similar good linear correlation is observed in Fig. 11 between the numerical results and the scaling prediction, which again confirms the previous scaling.

5.5. Power of instability over the entire domain

Having revealed the characteristics of the frequency modes of instability, the above sections have also shed some light on the variation of the power of instability with depth and offshore distance separately. For a more detailed panorama, Fig. 12 shows the contour of the standard deviation of the vertical velocity over the entire flow domain, which characterizes the strength of thermal plumes.

The variation of the strength of the flow instability with the Rayleigh number is revealed through a comparison between Fig. 12(a) and (b). It is clear that both the strength and horizontal extent of instability increase with the Rayleigh number. A scaling relation for the horizontal extent of instability is proposed in the

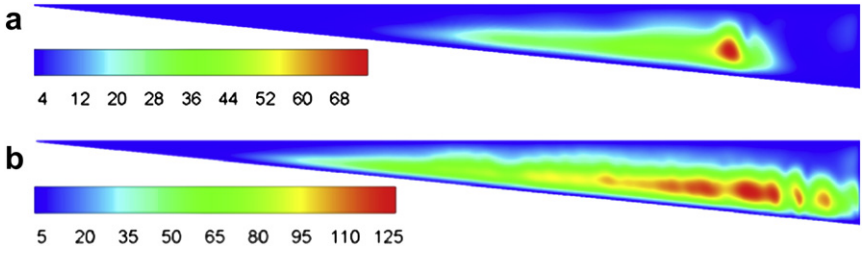

Fig. 12. Standard deviation of vertical velocity over the entire domain (a) $Ra = 1.4 \times 10^6$, (b) $Ra = 1.4 \times 10^7$.

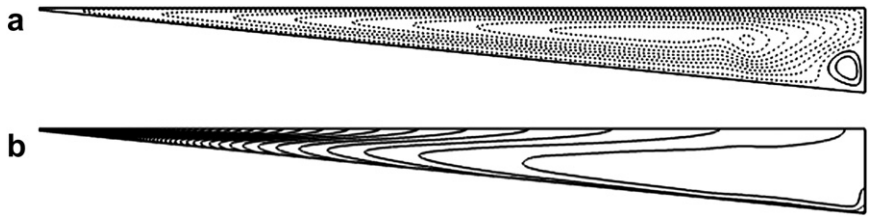

Fig. 13. (a) Streamlines and (b) isotherms of the mean flow at quasi-steady state for $Ra = 2.1 \times 10^6$.

previous investigation [17] and validated both in [17] and in the above section using different flow properties. Fig. 12 demonstrates that, for a given Rayleigh number, the strength of the thermal plumes decreases toward the shore, whereas it first increases and then decreases from bottom up. A boundary layer adjacent to the bottom slope with a very low power of instability can be clearly identified, and the thickness of this layer decreases with the increasing Rayleigh number. For relatively low Rayleigh numbers as shown in Fig. 12(a), thermal plumes are not sufficiently strong to break up the stable stratification in a layer underneath the water surface formed due to direct absorption of radiation, whereas for relatively high Rayleigh numbers such as the case shown in Fig. 12(b), thermal plumes reach positions closer to the water surface, indicating that thermal plumes plays a significant role in the vertical transport of nutrients and pollutants at relatively high Rayleigh numbers.

5.6. Scaling of the mean flow

The above discussed standard deviation is a measure of a quasi-steady fluctuating flow associated with flow instability superimposed on a time-averaged mean flow. By averaging a time series of the quasi-steady state flow, the fluctuation of flow properties caused by the thermal plumes can be smoothed out in the mean flow, and thus the unstable region becomes spuriously stable and can be regarded as an extension of the stable convection region. This is demonstrated in Fig. 13, which plots streamlines and isotherms of the mean flow averaged over a non-dimensional period of 0.12 during the quasi-steady state for $Ra = 2.1 \times 10^6$. By comparing Fig. 13 with Fig. 3, it is clear that the spatial patterns of the instability represented by the wavy streamlines and isotherms in Fig. 3 have been smoothed out in the mean flow, except for a small region close to the end wall which is subjected to the end wall effect.

The previous study of Mao et al. [17] has proposed and verified the scaling relations for both the conduction-dominated region and the region dominated by stable convection, which reveal the dependency of flow properties on the horizontal position x. However, the unstable convection region is not covered in the previous validation. In fact, a time series of any flow property in the unstable region at the quasi-steady state can be decomposed into a stable mean component and a regularly fluctuating component which is caused by the flow instability. It is expected that the scaling for convection dominated region is also applicable to the time-averaged mean flow of the unstable region. To validate this, the maximum velocities along vertical lines at different horizontal positions within the convection-dominated region, including the stable convection region and the unstable convection region (for high Rayleigh numbers only), are obtained from the mean flow and are plotted in Fig. 14 against the non-dimensional form of the scaling prediction specified by Mao et al. [17], which is

$$u \sim (x/h)^{1/3} e^{-1/3Ax\eta} Ra^{1/3} \tag{22}$$

after normalization by k/h. The data of the first three lower Rayleigh numbers for the stable-convection-dominated region in Fig. 14 are taken from the previous study [17]. It is clear that the scaling obtained for stable-convection-dominated region is also applicable to the mean flow of the unstable region. In other words, the mean flow of the unstable region can be regarded as an extension of the flow of the stable-convection-dominated region.

As specified in (22), the horizontal velocity of the mean flow increases with both Ra and the offshore distance x if $x < 1/(A\eta)$, i.e. $h < 1/\eta$, and thus the magnitude of horizontal flow exchange increases along the offshore direction in the near shore shallow water where $h < 1/\eta$. As the strength and frequency of vertical mixing through thermal plumes also increase in the offshore

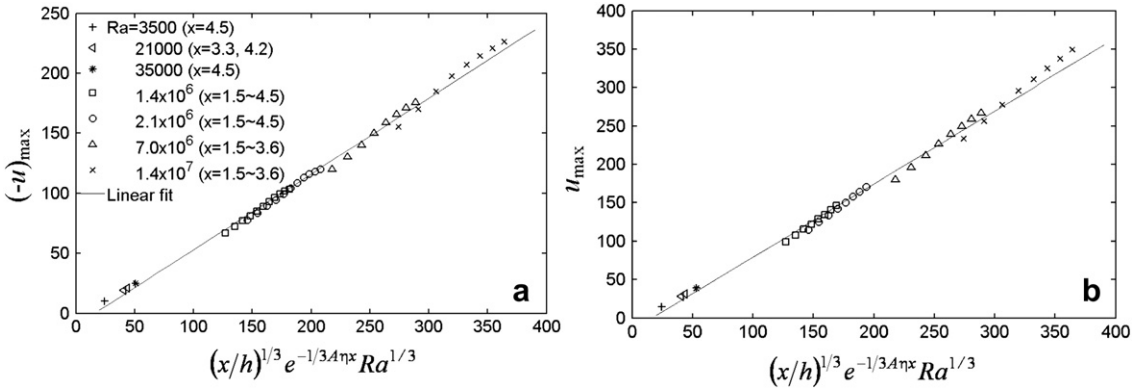

Fig. 14. Maximum horizontal velocity extracted along vertical lines at different horizontal positions within the convection dominated region (extending to the unstable convection region for the last four Rayleigh numbers for which instability occurs) (a) Maximum negative horizontal velocity u in the bottom layer (b) Maximum horizontal velocity u in the upper layer. The horizontal positions are extracted at equal intervals within the specified range.

direction, the above results suggest an increasing dynamism of both horizontal exchange and vertical mixing of nutrients or pollutants in the offshore direction in shallow waters.

6. Conclusions

The present paper is a sequential investigation of the scaling analysis of Mao et al. [17]. For different flow regimes, the previous analysis has provided detailed scaling for identifying regions with distinct thermal flow characteristics. For the unstable flow regime, the entire flow domain is divided into three distinct sub-regions along the offshore direction: a conduction-dominated region, a stable-convection-dominated region and an unstable convection region. The criteria for instability to occur and the extent of unstable region are revealed in the scaling, which forms the basis of the present investigation. The previous paper has validated the scaling for the conduction-dominated region and the stable-convection-dominated region using numerical data. For unstable region, the present paper reveals that the mean flow of the unstable region averaged over the quasi-steady state is scaled the same as the stable-convection-dominated region, indicating an increasing time-averaged horizontal exchange in the offshore direction.

From the spatial perspective, the isotherms and streamlines at the quasi-steady state reveal the spatial patterns of instability as thermal plumes rising up from the bottom. From the temporal perspective, characteristics of flow instability at the quasi-steady state in near shore waters are investigated by the spectral analysis of the time series of various flow properties, which has revealed the spectra variation with water depth, offshore distance and the Rayleigh number. In this way, a detailed picture is provided for the frequency modes and strength of flow fluctuations over the entire domain.

For a fixed offshore distance, spectral analysis suggests that the frequency modes are the same at different depths. However, the dominancy of higher frequency modes increases with water depth. The strongest power of vertical mixing occurs near the sloping bottom. In the offshore direction, the strength of fluctuation increases and higher frequency modes become increasingly pronounced. As the Rayleigh number increases, the number of frequency modes, the highest dominant frequency and the strength of fluctuation increase. Harmonic frequency modes are present for relatively low Rayleigh numbers. As the Rayleigh number increases, the interaction between different frequency modes becomes stronger and the spectrum deviates from harmonic modes.

Stability of the buoyancy driven flow investigated in this paper belongs to a broad class of stability problem in both nature and industry. The present investigation sheds light on the characteristics of exchange and mixing induced by the absorption of solar radiation in near shore waters, which has significant implications on the transport of terrestrially derived particulates and solutes. In addition to the increasing time-averaged horizontal exchange along the offshore direction indicated by the velocity scaling, results of the present investigation suggest that in shallow waters, the radiation-induced mixing becomes stronger with increasing frequencies as the offshore distance and/or the Rayleigh number increases. As the Rayleigh number increases, the unstable region extends toward the shore; meanwhile, the thermal plumes penetrate closer to the water surface, indicating an increasing dynamism of vertical mixing.

It is worth noting that the present investigation considers only the radiation-induced instability in the near-shore shallow water region ($h < 1/\eta \sim 1$–2 m), where the heat flux resulting from the absorption of radiation by the sloping bottom is strong. Coupling of the radiation-induced instability in the shallow region discussed here with the stable stratification in the far offshore region and instability generated by other processes, such as wind generated waves [1] will provide a more comprehensive picture of instability in near shore waters.

Acknowledgements

The authors gratefully acknowledge the financial support of the Australian Research Council. This work was carried out while Yadan Mao was a recipient of a PhD scholarship jointly awarded by China Scholarship Council and James Cook University.

References

[1] Y. Mao, M.L. Heron, The influence of fetch on the response of surface currents to wind studied by HF ocean surface radar, J. Phys. Oceanogr. 38 (2008) 1107–1121.
[2] H.B. Fischer, J.E. List, C.R. Koh, J. Imberger, N.H. Brooks, Mixing in Inland and Coastal Waters, Academic, 1979.
[3] J. Imberger, J.C. Patterson, Physical limnology, Adv. Appl. Mech. 27 (1990) 303–475.
[4] J. Imberger, Physcial Processes in Lakes and Oceans, American Geophysical Union, 1998.
[5] E.E. Adams, S.A. Wells, Field measurements on side arms of lake, J. Hydraulic Eng. 110 (1984) 773–793.
[6] S.G. Monismith, J. Imberger, M.L. Morison, Convective motions in the siderarm of a small reservoir, Limnol. Oceanogr. 35 (1990) 1676–1702.
[7] S.G. Monismith, A. Genin, M.A. Reidenbach, G. Yahel, J.R. Koseff, Thermally driven exchanges between a coral reef and the adjoining ocean, J. Phys. Oceanogr. 36 (2006) 1332–1347.
[8] H. Niemann, C. Richter, H.M. Jonkers, M.I. Badran, Red Sea gravity currents cascade near-reef phytoplankton to the twilight zone, Mar. Ecol. Prog. Ser. 269 (2004) 91–99.
[9] S.G. Monismith, Hydrodynamics of Coral Reefs, Annu. Rev. Fluid Mech. 39 (2007) 37–55.
[10] W.F. James, J.W. Barko, Estimation of phosphorus exchange between littoral and pelagic zones during nighttime convective circulation, Limnol. Oceanogr. 36 (1991) 179–187.
[11] W.F. James, J.W. Barko, H.L. Eakin, Convective water exchanges during differential cooling and heating: implications for dissolved constituent transport, Hydrobiologia 294 (1994) 167–176.
[12] C.B. Lövstedt, L. Bengtsson, Density-driven current between reed belts and open water in a shallow lake, Water Resources Res. 44 (2008) W10413. doi:10.1029/2008WR006949.
[13] D.E. Farrow, J.C. Patterson, On the response of a reservoir sidearm to diurnal heating and cooling, J. Fluid Mech. 246 (1993) 143–161.
[14] D.E. Farrow, Periodically forced natural convection over slowly varying topography, J. Fluid Mech. 508 (2004) 1–21.
[15] D.E. Farrow, J.C. Patterson, The daytime circulation and temperature structure in a reservoir sidearm, Int. J. Heat Mass Transfer 37 (1994) 1957–1968.
[16] C. Lei, J.C. Patterson, Unsteady natural convection in a triangular enclosure induced by absorption of radiation, J. Fluid Mech. 460 (2002) 181–209.
[17] Y. Mao, C. Lei, J.C. Patterson, Unsteady natural convection in a triangular enclosure induced by absorption of radiation – a revisit by improved scaling analysis, J. Fluid Mech. 622 (2009) 75–102.
[18] C. Lei, J.C. Patterson, Natural convection in a reservoir sidearm subject to solar radiation: experimental observations, Exp. Fluids 32 (2002) 590–599.
[19] C. Lei, J.C. Patterson, Natural convection induced by diurnal heating and cooling in a reservoir with slowly varying topography, JSME Int. J. Ser. B 49 (2006) 605–615.
[20] D.E. Farrow, J.C. Patterson, On the stability of the near shore waters of a lake when subject to solar heating, Int. J. Heat Mass Transfer 36 (1993) 89–100.
[21] C. Lei, J.C. Patterson, A direct stability analysis of a radiation-induced natural convection boundary layer in a shallow wedge, J. Fluid Mech. 480 (2003) 161–184.
[22] J.R. Lloyd, E.M. Sparrow, On the stability of natural convection flow on inclined plates, J. Fluid Mech. 42 (1970) 465–470.
[23] J.E. Hart, Stability of the flow in a differentially heated inclined box, J. Fluid Mech. 47 (1971) 547–576.
[24] J.N. Shadid, R.J. Goldstein, Visualization of longitudinal convection roll instability in an inclined enclosure heated from below, J. Fluid Mech. 215 (1990) 61–84.
[25] C. Lei, J.C. Patterson, Two- and three-dimensional temperature structure in a shallow wedge subject to solar radiation, in: Proceedings of 14th Australasian Fluid Mechanics Conference, Adelaide, Australia, 2001, vol. I, pp. 359–362.
[26] A. Rabl, C.E. Nielsen, Solar ponds for space heating, Solar Energy 17 (1975) 1–12.
[27] U.H. Kurzweg, Stability of natural convection within an inclined channel, Trans. ASMEC: J. Heat Transfer 92 (1970) 190–191.